Computational analysis of the flowfield past a returning capsule at super-orbital speed

*Antonio Viviani * and Giuseppe Pezzella ***
** Seconda Università di Napoli (SUN)*
via Roma 29, 81031 Aversa, Italy
*** Centro Italiano Ricerche Aerospaziali (CIRA)*
via Maiorise, 81043 Capua, Italy

Abstract

This paper deals with the computational fluid dynamics analysis of a capsule entering the Earth atmosphere at the end of a sample return mission. Several numerical simulations have been carried out to assess the flowfield environment past a sphere-cone capsule, by using non-equilibrium reacting gas approximations. Heat shield ablation and effects of flow plasma radiation on capsule aeroheating are also accounted for in the flowfield analysis. The issue of aerodynamic and aerothermodynamic performance of the entry spacecraft in the framework of a super-orbital re-entry scenario is addressed.

1. Introduction

The capability to send vehicles into space with the aim of collecting samples from Planets (i.e. Mars) and other celestial bodies represents an important step forward for Space Exploration activities and for a more accurate knowledge of the Earth and Universe. In this framework the capability to address computational flowfield analysis past a capsule returning at super-orbital speed is fundamental. In fact, these extra-terrestrial samples have to be returned to Earth, and very high-speed re-entry trajectories must be performed by the space vehicles, according to Celestial Mechanics laws. Therefore, the design of an Earth entry sample return vehicle (SRV) requires strong technological bases and has to rely on a good understanding of the loading environment encountered during the super-orbital Earth re-entry. A high speed Earth entry vehicle has the following characteristics: entry velocity higher or equal to 11.7 km/s (compared to 7.5 km/s for the US Space Shuttle); very high heat fluxes (more than 10 MW/m^2) and heat loads (in the range of 200 MJ/m^2), where the radiative part is rather important.

In this framework a capsule configuration has been selected and a re-entry trajectory has been computed to address the SRV aerodynamic and aerothermodynamic analysis.

2. Capsule configuration and flight scenario

Trade-off design analysis among hypersonic drag (heating), subsonic drag (impact velocity) and subsonic stability (available crush stroke) suggests to consider a sphero-conical capsule aeroshape with a 45 deg half cone angle, a 1.1 m diameter front shield, a nose radius equal to 0.275 m, a shoulder radius of curvature equal to 0.0275 m and a smaller back-cover (Figure 1) [1]. The capsule vehicle, including margins, is estimated to weigh about 50 kg with the center of gravity (CoG) at 26.9% from the nose relatively to the SRV diameter. This layout and design of the SRV assure a safe return of the sample canister, relying on a fully passive concept [1].

The flight design scenario of the SRV concept is shown in Figure 2. It refers to an Earth descent characterized by -12.5 deg of flight path angle, 12.3 km/s of entry velocity at 120 km altitude and, therefore, by a rather high heat flux peak. The evolutions of heat fluxes (convective and radiative part) with the corresponding integrated heat load are also presented in Figure 2.

In the preliminary design the convective and radiative heat fluxes were estimated by using analytical engineering correlations such as Scott relationship for convective heat flux and Tauber-Sutton one for the radiative heat flux evaluation [2,3]. All the preliminary estimations provided in Figure 2 are extremely important for designing the capsule. Indeed, the descent trajectory provides initial conditions for CFD solutions while the aeroheating environment dictates the type and size of the thermal protection system (TPS) to be used. Peak heat rate generally determines the range of possible thermal protection material (TPM) while the integrated heat load determines the thickness and hence the mass of the capsule heat shield.

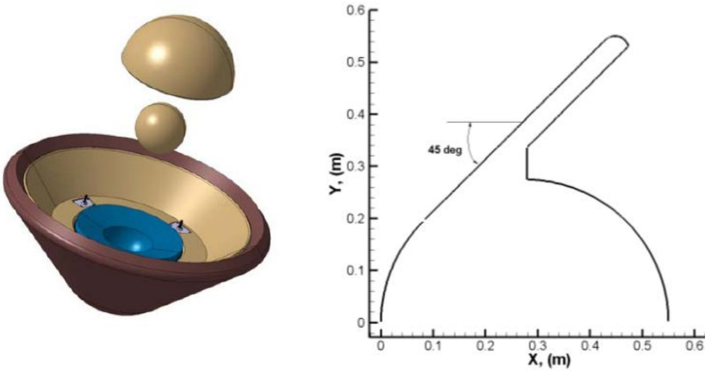

Figure 1: Capsule geometry with quotes

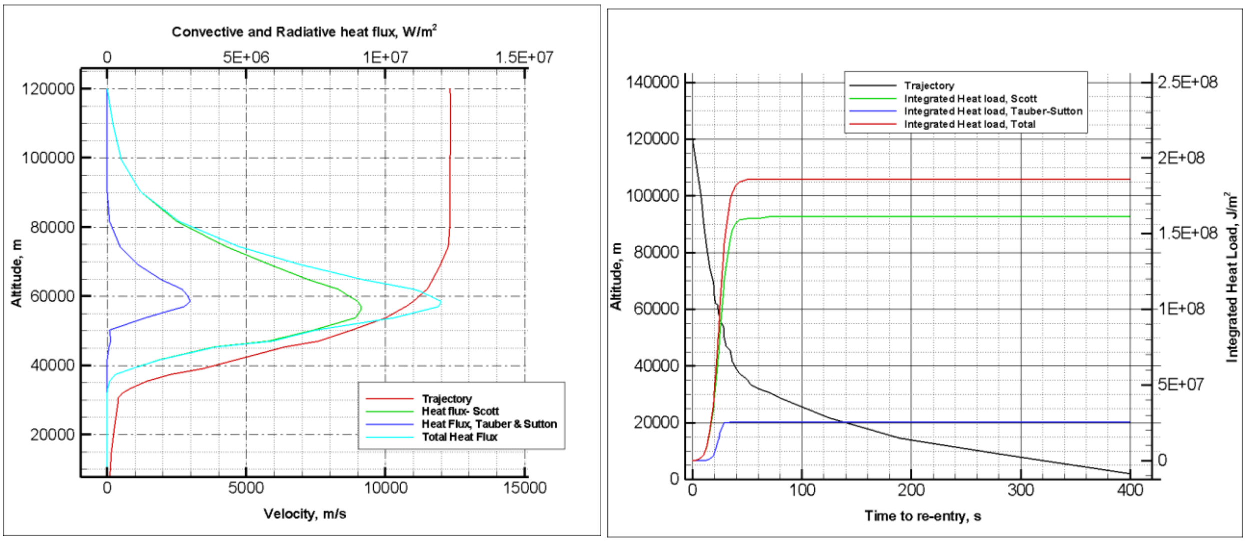

Figure 2: Re-entry trajectory in the altitude-velocity map and aerothermal loading conditions

3. Capsule aerodynamic and aerothermodynamic performance analysis

The appraisal of the aerodynamic and aerothermodynamic characteristics of the SRV concept is performed. These evaluations are aimed to address the aerothermal loads the vehicle has to withstand during re-entry at super-orbital speed. To this aim a number of extreme loading flight conditions has been focused along with the sizing flight trajectory, according to the trajectory-based design approach. The heat flux distributions, both convective and radiative one, are also addressed for each chosen trajectory design point provided that planetary entries, and particularly sample return missions, are often characterized by strong radiation and ablation effects. However, it is worth noting, that due to the prohibitive computational effort, no fully coupled computations of heat shield ablation and flow plasma radiation were undertaken in this work.

In the present analysis only continuum regime (between Mach 3 and Mach 41.54) with the air modelled as a mixture of several gases (including also those coming from heat shield ablation) has been analysed.

In particular, the appraisal of the vehicle aerodynamic and aerothermodynamic was performed by means of both engineering-based tools and Navier-Stokes (NS) CFD computations in thermo-chemical non-equilibrium and both laminar and turbulent flow conditions. Then, results of CFD simulations are provided to PARADE code for the estimation of the radiative heat fluxes the capsule has to withstand during the super-orbital re-entry flight [4].

Engineering based aerodynamic analyses were extensively performed by using a 3D Panel Method code developed by CIRA (SIM–Surface Impact Method) [5]. This tool at high supersonic and hypersonic speeds is able to accomplish the aerodynamic and aerothermodynamic analyses of a complex re-entry vehicle configuration by using simplified approaches as local surface inclination methods and approximate boundary-layer methods, thus avoiding the time consuming and complex grid generation phase and the computation processes of a CFD analysis. The vehicle surface is approximated by a system of planar panels. The methods to be used to calculate the pressure on each panel of impact and shadow regions may be specified independently and can be selected by the user. The shear force is determined on each capsule panel in order to assess the viscous contribution of the aerodynamic forces and moments. The skin friction is estimated based on the assumption of a laminar or turbulent flat plate. Reference temperature and enthalpy methods are available for both laminar and turbulent flows. The viscous calculation is performed along streamlines, and the results are then interpolated to the panel centroids.

The numerical tool used to carry out the CFD analyses is the CIRA code H3NS/CAST [6]. It solves the flowfield governing equations, including chemical and vibrational non-equilibrium, with a finite volume approach. The fluid is treated as a mixture of perfect gases and the energy exchange between vibrational and translational modes (TV) is modelled with the classical Landau-Teller non-equilibrium equation, with average relaxation times taken from the Millikan-White theory modified by Park. As far as the transport coefficients is concerned, the viscosity of the single species is evaluated by a fit of collision integrals calculated by Yun and Mason, the thermal conductivity is calculated by means of the Eucken law; the viscosity and thermal conductivity of the gas mixture are then calculated by using the semi-empirical Wilke formulas. The diffusion of the multi-component gas is computed through a sum rule of the binary diffusivities of each couple of species (from the tabulated collision integrals of Yun and Mason). Transport coefficients, in the hypothesis of an ideal gas, are derived from Sutherland law, suitably modified to take into account for low temperature conditions. With respect to the numerical formulation, conservation equations, in integral form, are discretized with a finite volume, cell centred, technique. Eulerian fluxes are computed with a flux difference splitting upwind scheme. Second order formulation is obtained by means of an ENO-like reconstruction of cell interface values. Viscous flux is computed with a classical centred scheme i.e. computing the gradients of flow variables at cell interfaces by means of Gauss theorem. Integration in time is performed by employing an explicit multistage Runge-Kutta algorithm coupled with an implicit evaluation of the species and vibration energies source terms. Also a parallel version of the code is currently available.

The flow radiative heat flux at the SRV wall has been computed through the code PARADE, starting from the results of the fluid dynamic computations (in terms of gas composition and temperature) [4]. This code is able to compute flow-field emission and absorption, between the shock layer and the surface of the probe. The spectral emission and absorption are determined as function of transition level (from upper level to lower level) and emitting population of this level. The population can be derived from the Quasi-Steady-State (QSS) method or by a Boltzmann method in order to take into account for the non-equilibrium or equilibrium regime, respectively. The radiative computations have been performed with the Boltzmann assumption for the determination of the population of the excited molecular states.

The radiative heat transfer equation (RTE) has been solved using the one dimensional tangent slab approximation (radiation properties are assumed to vary only in the direction normal to the wall). The intensity of radiation at a given wavelength λ satisfied the equation of radiative transfer:

$$\frac{\partial I_\lambda}{\partial s} = j_\lambda - k_\lambda I_\lambda \tag{1}$$

where j_λ and k_λ are respectively the emission and absorption coefficients, computed through PARADE. These coefficients are integrated along with straight lines toward the wall according to the above equation to compute I_λ. Radiative heat flux at a given wavelength λ is then obtained through integration of I_λ over the solid angle whereas the total radiative heat flux is obtained through integration over the spectrum of interest. In particular, a spectral region between 100 and 40000 nm using 50000 spectral grid locations has been considered in the calculations.

3.1 Loading conditions scenario and air mixture composition

SRV aerothermal analyses refer to CFD simulations performed at the several discrete points of the flight scenario summarized in Figure 3 and Table 1, where free stream conditions of design points are provided. Therefore, fifteen trajectory points (TP) have been considered to perform 19 NS thermo-chemical non-equilibrium simulations. Furthermore, to take an idea of real gas effects that the capsule will experience during descent, Figure 3 also shows the re-entry trajectory superimposed on the fields (from 10% to 90 %) of vibrational excitation (VE), Oxygen and Nitrogen dissociation (OD and ND), and ionization (I) of flow species [7].

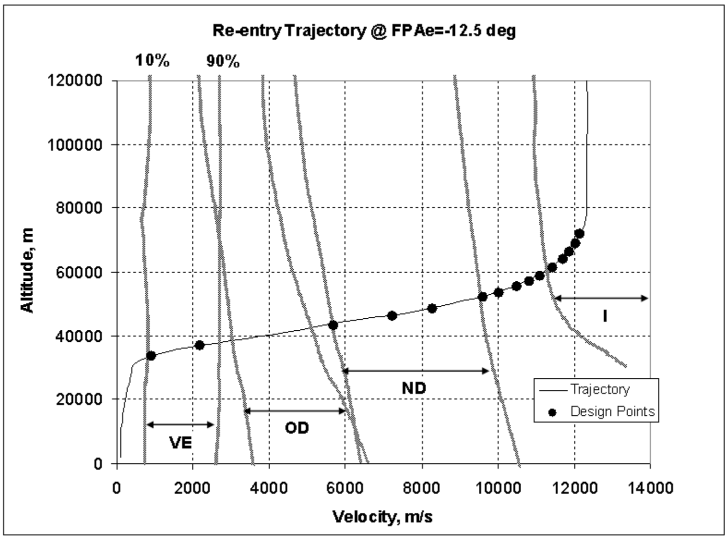

Figure 3: Re-entry trajectory in the altitude-velocity map with design point

Table 1: Design points

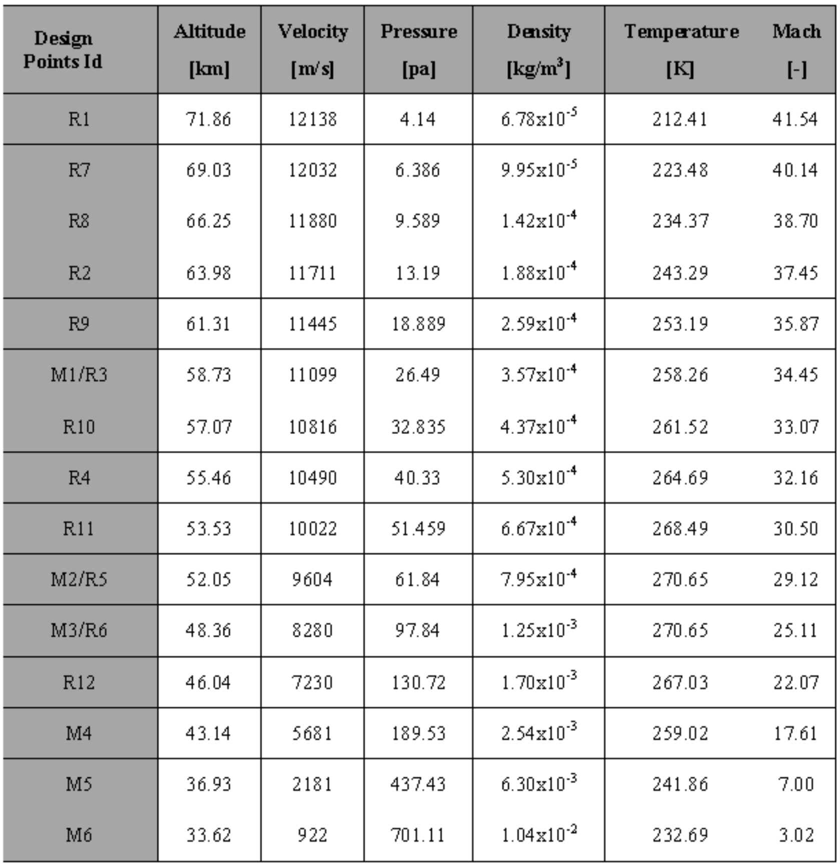

Design Points Id	Altitude [km]	Velocity [m/s]	Pressure [pa]	Density [kg/m^3]	Temperature [K]	Mach [-]
R1	71.86	12138	4.14	6.78×10^{-5}	212.41	41.54
R7	69.03	12032	6.386	9.95×10^{-5}	223.48	40.14
R8	66.25	11880	9.589	1.42×10^{-4}	234.37	38.70
R2	63.98	11711	13.19	1.88×10^{-4}	243.29	37.45
R9	61.31	11445	18.889	2.59×10^{-4}	253.19	35.87
M1/R3	58.73	11099	26.49	3.57×10^{-4}	258.26	34.45
R10	57.07	10816	32.835	4.37×10^{-4}	261.52	33.07
R4	55.46	10490	40.33	5.30×10^{-4}	264.69	32.16
R11	53.53	10022	51.459	6.67×10^{-4}	268.49	30.50
M2/R5	52.05	9604	61.84	7.95×10^{-4}	270.65	29.12
M3/R6	48.36	8280	97.84	1.25×10^{-3}	270.65	25.11
R12	46.04	7230	130.72	1.70×10^{-3}	267.03	22.07
M4	43.14	5681	189.53	2.54×10^{-3}	259.02	17.61
M5	36.93	2181	437.43	6.30×10^{-3}	241.86	7.00
M6	33.62	922	701.11	1.04×10^{-2}	232.69	3.02

In particular, CFD computations are in turbulent flow conditions for points below 51.9 km altitude. Note that, for the determination of the laminar-to-turbulent (L/T) transition the simplest estimate is made from free-stream Reynolds number and here we use a critical value of $5.0x10^5$ based on diameter, as made in the past for the ARD post-flight data.

$$Re_{\infty,D} = \left(\frac{\rho_\infty u_\infty D}{\mu_\infty}\right) \geq 5.0x10^5 \tag{2}$$

The atmosphere composition is considered made of: Y_{N2}=0.75548; Y_{O2}=0.23161, and Y_{Ar}=0.01291. Therefore, the specific gas constant for air is $R_{air}=R_0/M$=287.182 J/Kg/K. The model proposed for the air mixture is constituted by 13 species: Molecules: N_2, O_2, NO; Atoms: N, O, Ar; Ions: $N2^+$, $O2^+$, NO^+, N^+, O^+, Ar^+ and e^-; while to account for heat shield blowing mass the air mixture consists of 32 species: Molecules: N_2, O_2, NO, C_2, H_2, C_3, C_2H_2, C_2H, CO_2, H_2O, CN, CH, NH, HCN, OH, CO; Atoms: N, O, Ar, C, H; Ions: N_2^+, O_2^+, NO^+, N^+, O^+, CN^+, CO^+, C^+, H^+, Ar^+ and e^-. The chemical model is based on Park [8]. It is constituted, when mass blowing is off, of 13 species and 22 chemical reactions that account also for third body efficiency. When heat shield species diffuse in the shock layer the chemical model is constituted of 67 chemical reactions which feature also the effect of collisional partner. For what concerns the thermal non-equilibrium model it is worth to note that a three temperature model is recommended: (T, T_v, T_e) [7-9]. T for translational and rotational mode for heavy species; T_v for vibrational modes, same temperature for all molecular species and T_e for translational mode of free electron.

In the present CFD computations, however, only two temperatures model for thermal non-equilibrium model (e.g., T and T_{vib}) has been considered. Vibrational relaxation is modelled using a Landau-Teller formulation, where relaxation times are obtained from Millikan-White with the high temperature correction due to Park [7-9].

Finally, flight regime assessment was made in order to be sure that all TPs lie within the flow continuum regime to be able to use CFD analysis, as discussed in the next paragraph.

3.2 Flight regime overview and flow simulation modelling

Generally speaking, along the atmospheric re-entry trajectory three main flow regimes can be recognized [9]. They are the hypersonic-supersonic regime, concerning the upper part of descent trajectory, the transonic and the subsonic regimes, regarding the flight within the lower atmospheric layers. Moreover, within the hypersonic regime two main and heavily overlapping regimes apply. They are the rarefied and the continuum regimes.

Once SRV vehicle started its descent, the atmospheric density is low enough that the molecular mean free path (δ) can become as large as the scale of the body itself. As a consequence, the continuum assumption does not apply.

This condition is known as Free Molecule Flow (FMF) regime and, the aerodynamic and aerothermodynamic characteristics of the capsule are determined by individual, scattered molecular impacts, and must be analysed on the basis of Kinetic Theory. Therefore, the SRV concept, moving from a very rarefied atmosphere (at entry interface) to a denser atmosphere, shifts from the FMF regime, where individual molecular collisions are important, to the transitional one, where slip effects are important, and then to the continuum regime, as represented in Figure 4.

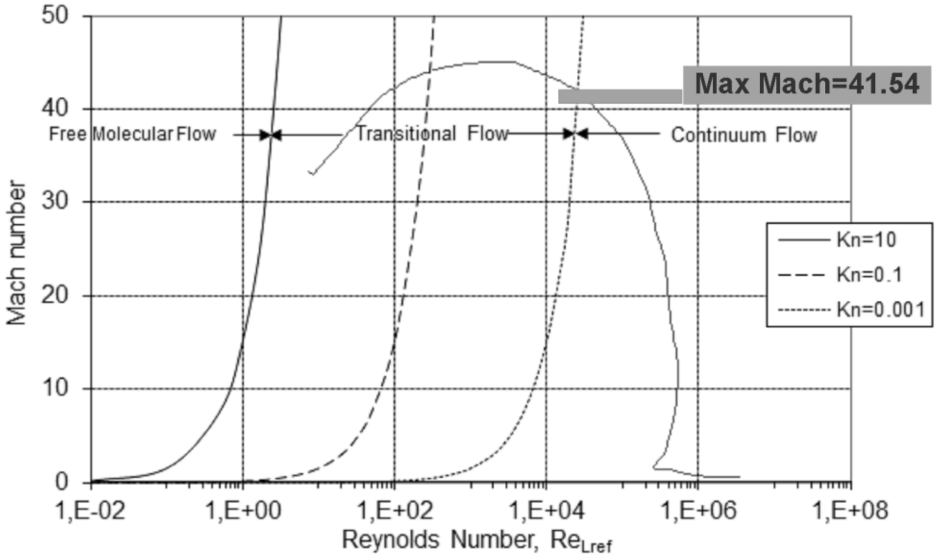

Figure 4: SRV re-entry trajectory in the Ma-Re map with constant Knudsen numbers

For instance, the similarity parameter that governs these different flow regimes is the Knudsen number, defined as (rarefaction parameter):

$$\mathrm{Kn}_{\infty L_{ref}} = \frac{\delta}{L_{ref}} = 1.25\sqrt{\gamma}\,\frac{M_{\infty}}{\mathrm{Re}_{\infty L_{ref}}} \tag{3}$$

where L_{ref} (i.e., 1.1 m – capsule diameter) is the characteristic length of the body. As shown in Figure 4, the maximum Mach number (i.e., 41.54) evaluated by the SRV Flight Mechanics analysis lies in the continuum flow regime. Therefore, all CFD computations have been performed with Navier-Stokes approximation without slip conditions at wall.

3.3 Computational domains, boundary conditions and solution convergence

CFD computations have been carried out on multiblock structured grids similar to those shown in Figure 5. As shown, two kinds of 2-D axis-symmetric computational domain have been considered for both whole and front shield domains, respectively.

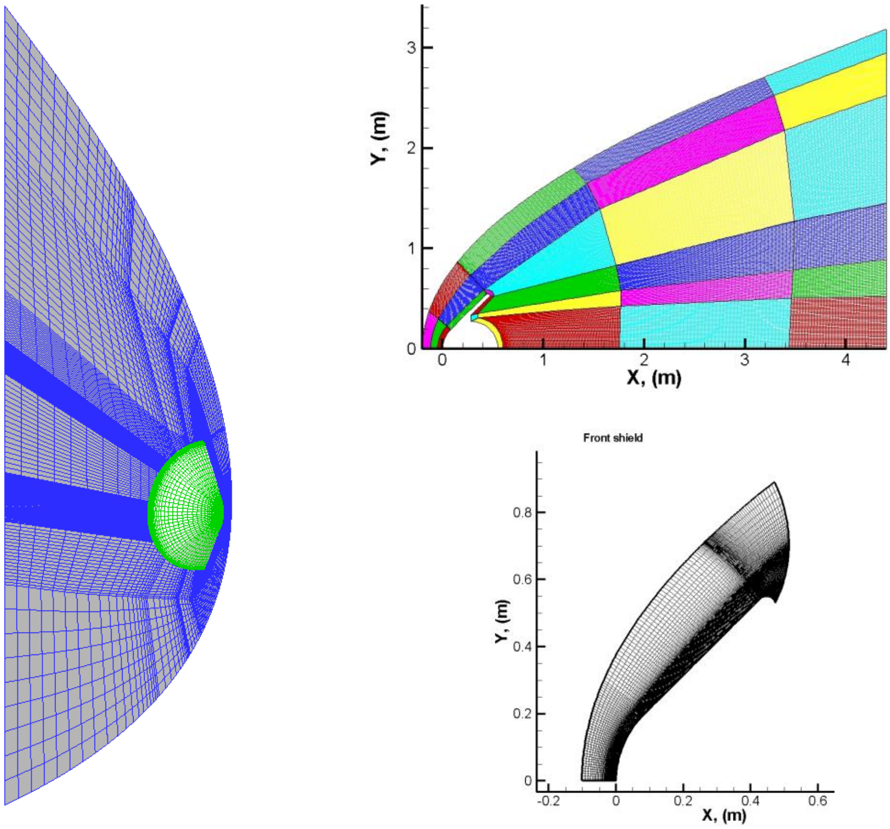

Figure 5. CFD multiblock computational domains.

The effective dimensions of the outflow boundary, axis and outer boundary are modified in each simulation in order to obtain a grid compliant to the flow-field conditions. The strategy adopted was to build the volume mesh be large enough to accommodate the freestream Mach number; while the distribution of grid points in the wall-normal direction is driven by freestream Reynolds number. Hence, the distribution of surface grid points was dictated by the level of resolution desired in various areas of vehicle such as stagnation region and base fillet, according to the computational scopes. For example, the grid has sufficient points in the shoulder region to capture the rapid expansion and accurately predict the flow separation point and the angle of the resulting shear layer. There are also enough points in the separated flow region to resolve the vortical structure at the beginning of the wake flowfield. Grid refinement in strong gradient regions of flowfield was made through a solution adaptive approach. As shown in Figure 5, grids for whole computational domain have an O-topology around the capsule in order to have blocks wrapping the SRV and with direction outgoing from the body wall, necessary for the boundary layer stretching. Three-dimensional computations are carried out on a mesh domain made of 48 blocks with about 800000 cells. The generic grid used for whole domain numerical calculations has consisted of about 30 blocks for an overall number of about 72000 cells (half body). The grid (front shield case) is constituted by 124x160 cells (longitudinal x normal to the wall direction) and assures fully spatially converged results. In particular, the mesh was initially generated algebraically and then adopted as the solution evolved. A local refinement has been done in the shock region in front of the capsule to better resolve the steep gradients, aligning the grid with the bow shock and clustering points into the boundary layer. This reduced the spurious oscillations in the stagnation area that are often observed in hypersonic flows, especially for large bluff-body flowfield computations. The minimum spacing at the wall is equal to 10^{-6} m to accurately predict heat transfer at the vehicle surface. When the flow is in turbulent conditions the values of the viscous coordinate y^{+} are less than 1.

All CFD results refer to both converged and grid independent computations. As far as wall boundary conditions are concerned, all simulations without heat shield ablation are performed with fully catalytic wall assumption i.e. chemical equilibrium at the wall to ensure the same wall conditions for all computations. In particular a wall temperature of T_W=1000 K (i.e., isothermal wall) has been also imposed. When heat shield mass diffuses in the shock layer, numerical simulations are carried out considering a prescribed mass fraction profile at wall for each blowing species. A wall temperature profile is also assumed at wall, as shown in Figure 6.

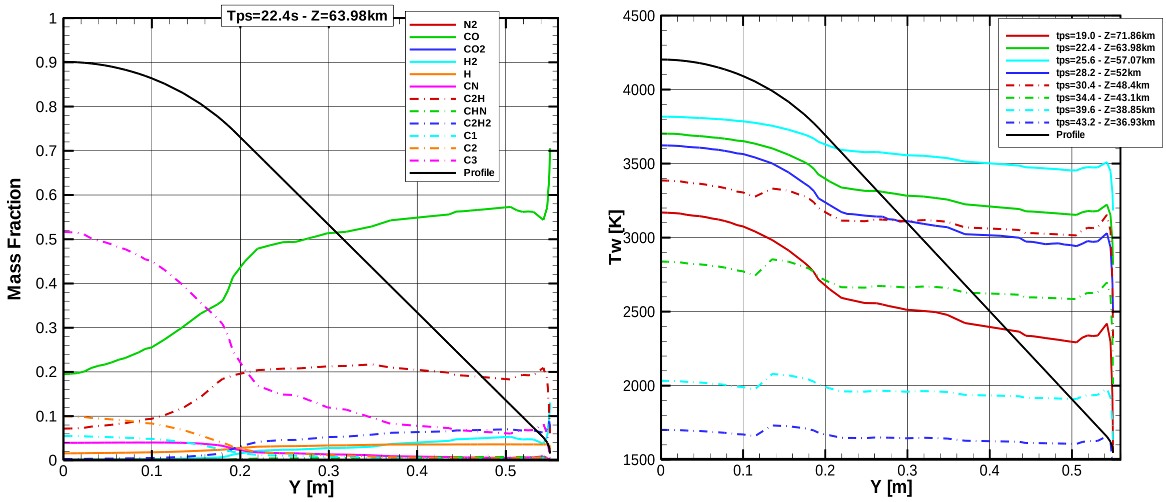

Figure 6. Mass fraction profiles at H_{∞}=63.98 km altitude and Temperature profile at different altitudes.

In order to assess numerical solution convergence, equation residuals and aerodynamic coefficient (i.e., C_D) as well as the stagnation point heat flux have been monitored during iterations. Solution convergence is assumed when equation residuals drop more than three orders of magnitude and both the aerodynamic coefficient and the stagnation point heat flux plots are flat for enough CFD iterations. For example, Figure 7 shows the aerodynamic and stagnation point heat flux convergence histories for the M1 simulation.

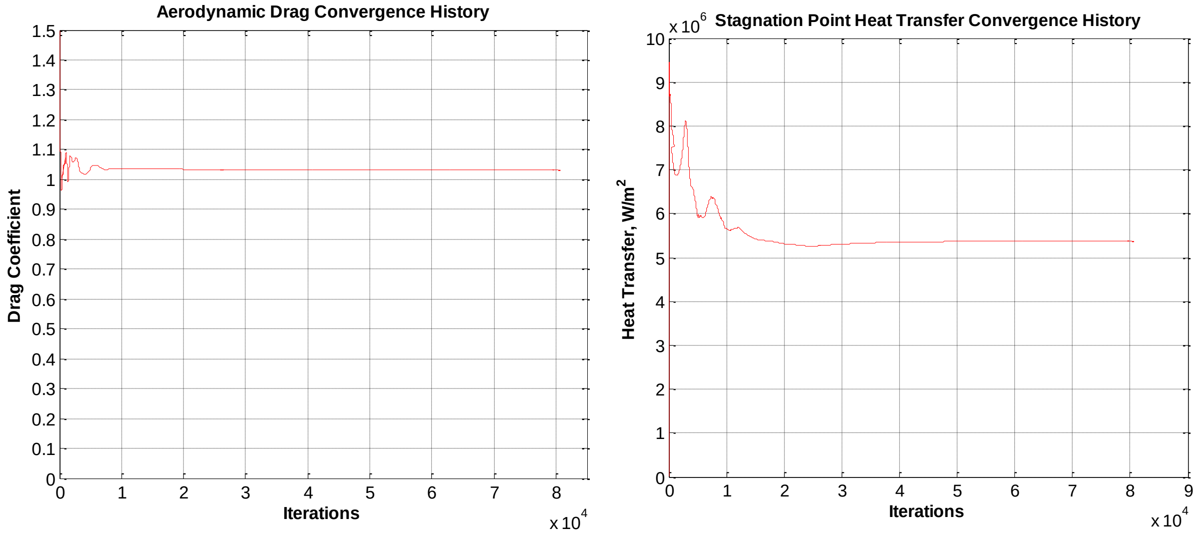

Figure 7. Drag coefficient and stagnation point heat flux vs iterations for R8 simulation.

3.4 Numerical results

Example of 3D numerical analysis can be found in Figure 8 and Figure 9. Three dimensional streamtraces, coloured by Mach number, past the capsule at M_∞=3 and α=10 deg and pressure distribution on the spacecraft front shield can be found in Figure 8.

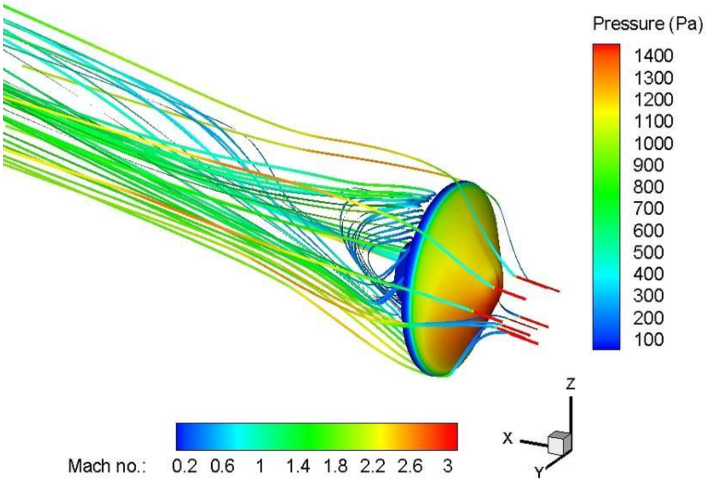

Figure 8. 3D streamtraces past SRV, coloured by Mach, and pressure field on heatshield at M_∞=3 and α=10 deg.

This figure provides very interesting flowfield features as the strong flow expansion at capsule shoulder and the complexity of the base flow. Figure 9 reports on the flowfield predicted around the SRV at M_∞=22.07 and 10 deg AoA. In particular, the figure shows the temperature contours provided both on the capsule pitch plane and two flowfield cross sections.

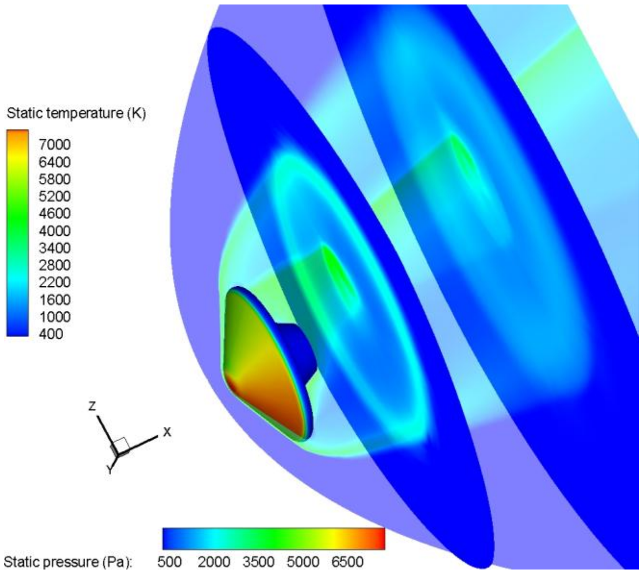

Figure 9. The static temperature field on the SRV pitch plane and on two cross sections at M_∞=22.07 and α=10 deg.

The pressure distribution over the SRV forebody is also provided. As shown, the maximum flowfield temperature is close to about 7000 K since, due to the high Mach number, thermo-chemical processes occur behind the bow shock as species vibrational excitation and dissociation, as discussed hereinafter. As shown in Figure 9, in the hypersonic portion of the re-entry, the flowfield is dominated by a strong bow shock and is characterized by all the typical hypersonic flowfield features as shock waves very close to the body surface (i.e., thin shock layer), thick boundary layers, high temperatures, and aerodynamic coefficients that can be nonlinear functions of angle of attack and etc [7,9]. As further example, temperature contours for M_∞=7 (M5 TP) are shown in Figure 10 for α=0 deg (e.g., axisymmetric 2D computations, whole domain).

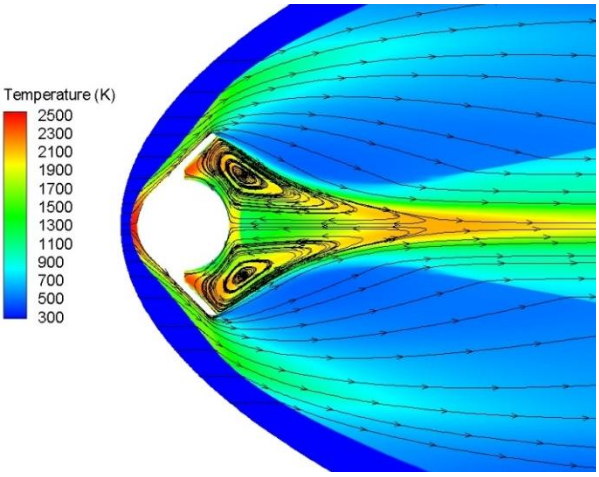

Figure 10. Temperature contours at M_∞=7.

As one sees, the flow crossing the bow shock suddenly decelerates thus increasing the pressure and temperature in the shock layer close to the stagnation region. The high angle of cone after the rounded stagnation region (equal to 45 deg) causes the curvature of the shock wave and, therefore, the presence of an entropy layer that affects the results at the wall (see Figure 15 and Figure 16). Further, the strong shock wave causes a large sonic region, a smooth conical flow along the SRV conical part, and a strong flow expansion at the shoulder. This expansion, dominated by inviscid effects, has the effect of rapidly lowering the translational temperature, density and pressure of the gas, while the chemical state of the gas and the temperatures, that characterize the energy in the internal modes, tend to remain frozen and the gas is still dissociated and excited. This aspect is very important by capsule aeroheating point of view. In fact, as the gas flows downstream, because of recombination occurs slowly, the vibrational temperature of gas rises still higher with the consequence that the gas can radiate significantly in the afterbody region. Streamlines are also shown in Figure in order to appreciate the flowfield structure surrounding the vehicle, especially the complexity of the wake flow. A strong base expansion together with a vortex feature can be appreciated as well. In particular, at the rearward facing base of the SRV the flow separates and creates a region of recirculating flow bounded by dividing streamlines. In fact, it is clearly shown the shear layer that starting from the SRV shoulder, converges on the capsule axis, undergoing normal shock at the neck of this flow to re-direct in the direction of the farfield. Hence, from neck flow it develops an oblique trailing shock wave, ultimately forming a viscous core or inner wake. Fluid in the inviscid wake crosses the trailing shock, increasing pressure, temperature, and density thereby, and in continuing downstream this outer wake merges with the inner wake.

The O_2 and N_2 mass fractions contours past the SRV are shown Figure 11.

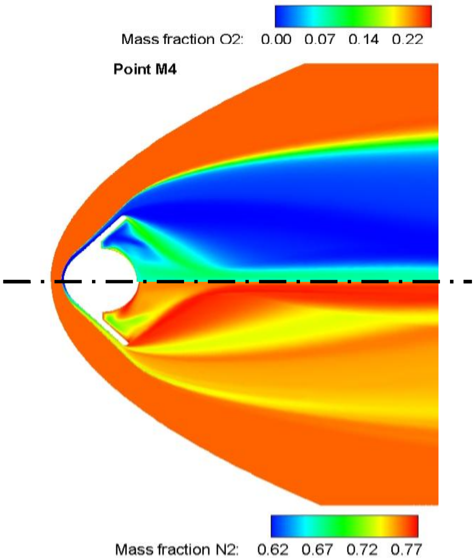

Figure 11. Species mass fractions contours field at M4 TP.

At this flight conditions the free stream Mach number is equal to 17.61. Therefore, a very strong shock wave detaches in front of the re-entering SRV. As a consequence, the air crossing the bow shock is suddenly heated and converted in a reacting mixture. As one can see, at these flight conditions the Oxygen completely dissociates while Nitrogen starts to dissociate.

Figure 12 shows the static pressure and Mach number front shield fields at M1 flight conditions.

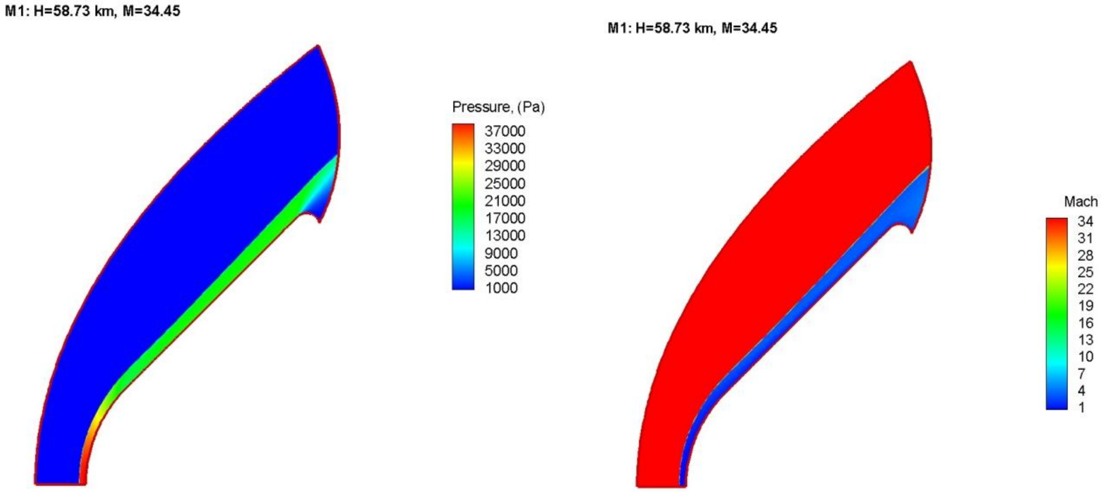

Figure 12. Static Pressure and Mach flowfields past SRV at M1 TP.

As shown, a very strong shock wave is generated in front the capsule due to the very high Mach number (i.e., M_∞=34.45). Indeed, as the capsule enters into the Earth's atmosphere directly from the hyperbolic Earth-return trajectory, the atmospheric entry speed of SRV is over 12 km/s (see Figure 2). Therefore, the shock layer gas is much more highly heated that the case of an Earth low orbital re-entry.

As a consequence, a large contribution to the vehicle aeroheating comes from the radiative heating of the plasma flow within the shock layer. This can be taken into account for the SRV TPS design.

Such a strong shock causes molecules of atmosphere to be dissociated and ionized, and consequently the gas in the shock layer consists of molecules, atoms, ions and electrons.

Temperature distributions along the capsule's stagnation line when the SRV is flying at M1 trajectory point are given in Figure13, in which translational and vibrational temperatures distributions are also highlighted.

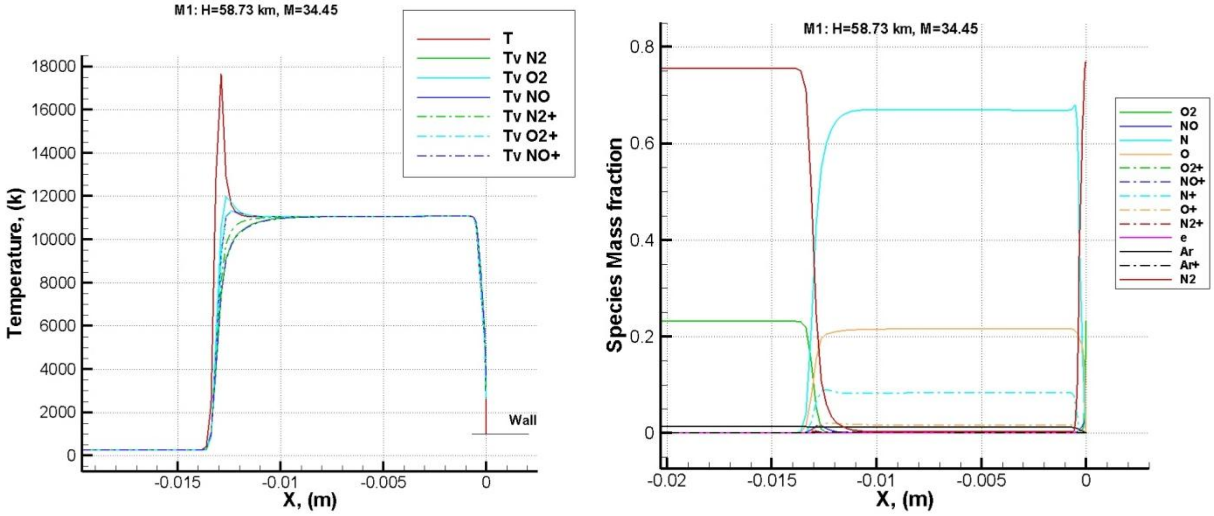

Figure 13. Temperatures and species mass fraction along with the stagnation line at M1 TP.

As one can see, the temperature behind the bow shock is very high thus causing the complete Oxygen and Nitrogen dissociation inside the shock layer, as shown by the right side of Figure13. Here, the distribution of the mass fraction of the neutral, ionized and ablation species along the stagnation line are reported. This figure points out that N_2 and O_2 molecules dissociate rapidly and, successively, the generation of NO molecule, the atomic Nitrogen and Oxygen, and the ionization of the molecules such as N_2, O_2 and NO, occur in the thermal non-equilibrium region. In general, the level of each formed species reaches a state of near chemical equilibrium for a large portion of the shock layer. Then, at the edge of the boundary layer the levels of the species start to change rapidly again as the temperature falls and the density rises through the boundary layer: N and O recombine to their molecular forms resulting in an increase in the levels of N_2 and O_2 and a fall in the levels of N and O. The reason for this is that the ionised species recombine with the electrons to form neutral species of N, O, N_2 and O_2, and NO, as shown in Figure 14.

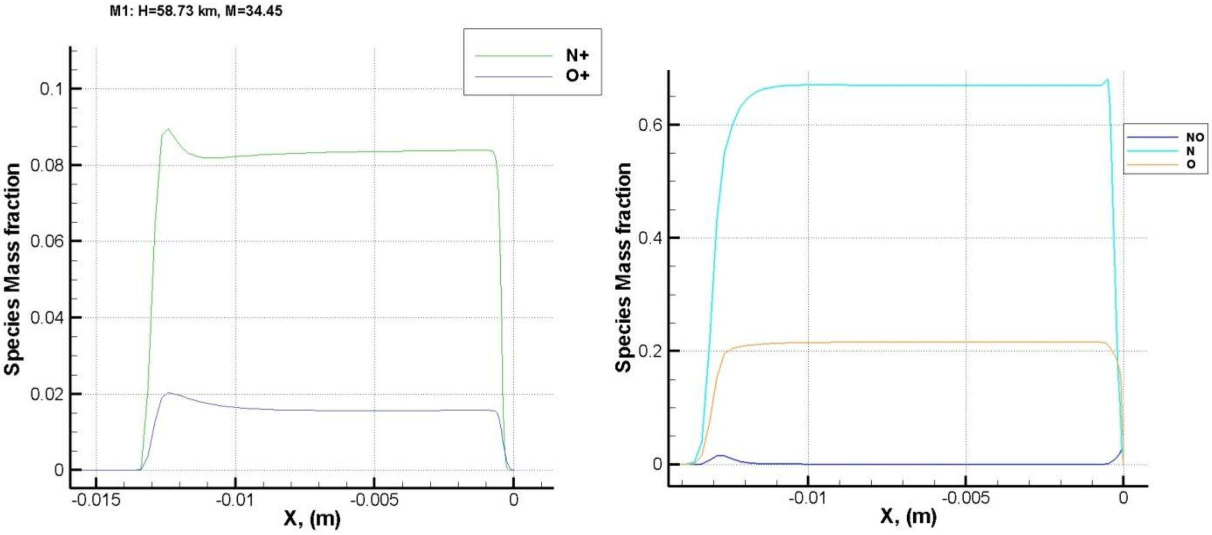

Figure 14. Species mass fractions along with the stagnation line at M1/R3 TP.

In particular, Figure13 and Figure 14 illustrate also that a large portion of the shock layer is in thermo-chemical equilibrium (i.e., the temperature profiles are quite flat until the boundary layer is reached) and only near the shock and in the boundary layer there is a departure from this state: the non-equilibrium region is just downstream the bow shock wave, and the size is of the order of the shock wave thickness. In fact, even if T_v increases much more slowly since it is density dependent, the two temperatures (T,T_v) are nearly equilibrated throughout the shock layer.

Moreover, the temperature trends exhibit a sharp discontinuity at the shock wave with a rapid decreasing behind the bow shock due to finite rate chemical reactions. For instance, the translational-rotational temperature, T, reaches the maximum value at about x=14 mm, while the vibrational-electronic temperature, T_v, is still much lower than T. T_v begins to be equilibrated around x=10 mm and continues to be equilibrated until the surface. On the contrary, the thermal non-equilibrium is observed at the region adjacent to the equilibrium one; i.e., from x=14 mm to 10 mm. The equilibrated temperature amounts up to about 11000 K.

Concerning the ionic species, there are substantial levels of O^+ and N^+ while the mass fractions of N_2^+, O_2^+ and NO^+ are very low. In fact crossing the shock, O_2 is rapidly and highly dissociated to form O and O^+. N_2 is dissociated to form N and NO by recombination with O but a small fraction of NO is created. A large part of the atomic nitrogen produced by the dissociation of N_2 is ionized in N^+. Figure 4 shows that the mass fractions of N^+ and O^+ amount up to around 0.085 and 0.015, respectively. Note that the ionisation process is very important considering that it has a non-negligible impact on radiative heat flux at high velocity flight conditions.

As far as SRV aeroheating (without accounting for heat shield ablation) is concerned, heat flux distributions at capsule front shield centreline for flight conditions ranging from R1 to R6 are shown in Figure 15. Results refer to convective and radiative heat fluxes at the wall. The latter one has been computed with PARADE with the density, the molar fractions and the two temperatures (translational and vibrational) of all the R trajectory points coming from CFD simulations.

As shown, Figure 15 highlights that the maximum radiative heat flux is equal to about 6 MW/m^2 and is reached at the R3/M1 flight conditions (i.e., H_∞=58.73 km altitude and M_∞=34.45). The convective peak heating reaches 8.5 MW/m^2, and it is attained at R5/M2 trajectory point (i.e., H_∞=52.05 km altitude and M_∞=29.12). Anyway, the maximum total heat flux is equal to about 12.5 MW/m^2 and it arises when the SRV is flying at H_∞=58.73 km altitude and M_∞=34.45 (i.e., R3/M1 TP). Therefore, plasma radiation is an additional contribution to surface aeroheating that must be taken into account in designing the SRV thermal protection system.

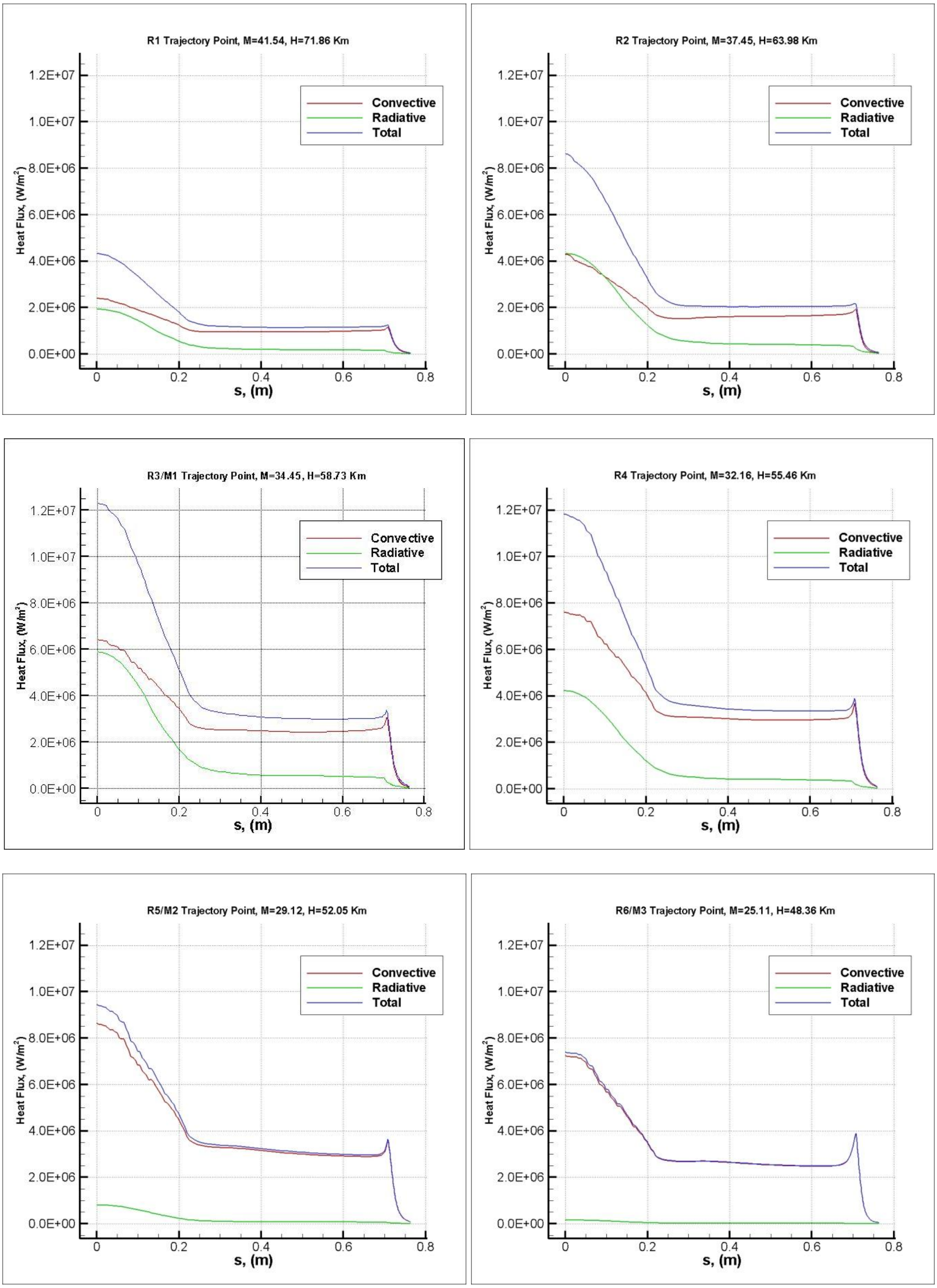

Figure 15. Convective and radiative heat fluxes comparison for R1-R6 TPs.

In particular, the generic convective heat flux profile in Figure 15 highlights that, after the peak at the stagnation point, the heat flux decreases along with the surface as the boundary layer develops up to an inflection point that corresponds at the end of the spherical shape of the capsule. Hence, it continues to decrease along with the conical part with a different shape and, then, it increases near the shoulder due to the small radius of curvature and to the expansion that causes a reduction of the boundary layer thickness.

Radiative heat flux profiles for the remaining R7 to R12 cases are quite the same as those of R1 to R6 reported in Figure5 and, therefore, are not reported for brevity.

The skin friction coefficient (C_f) over SRV centreline is summarized in Figure 16 for several trajectory points. As one can see, the peak of C_f is confirmed at the shoulder where boundary layer is extremely thin due to flow rotation around it.

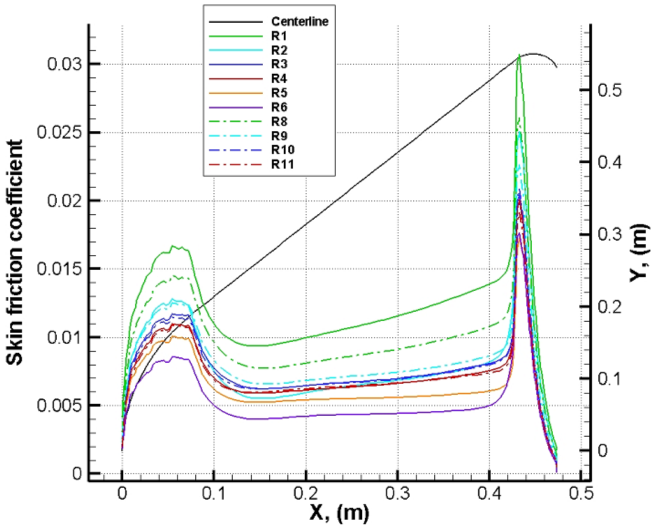

Figure 16. Skin friction coefficient for several R trajectory points.

The discussion of the results given previously for the non-ablating case is largely appropriate also for the flowfield analysis with mass blowing. For example, the Mach number and static pressure fields past the SRV front shield at R10/B3 TP (i.e., H_{∞}=57.07 km altitude and M_{∞}=33.07 at which occurs the maximum stagnation point total mass blow rate) are recognized in Figure 17.

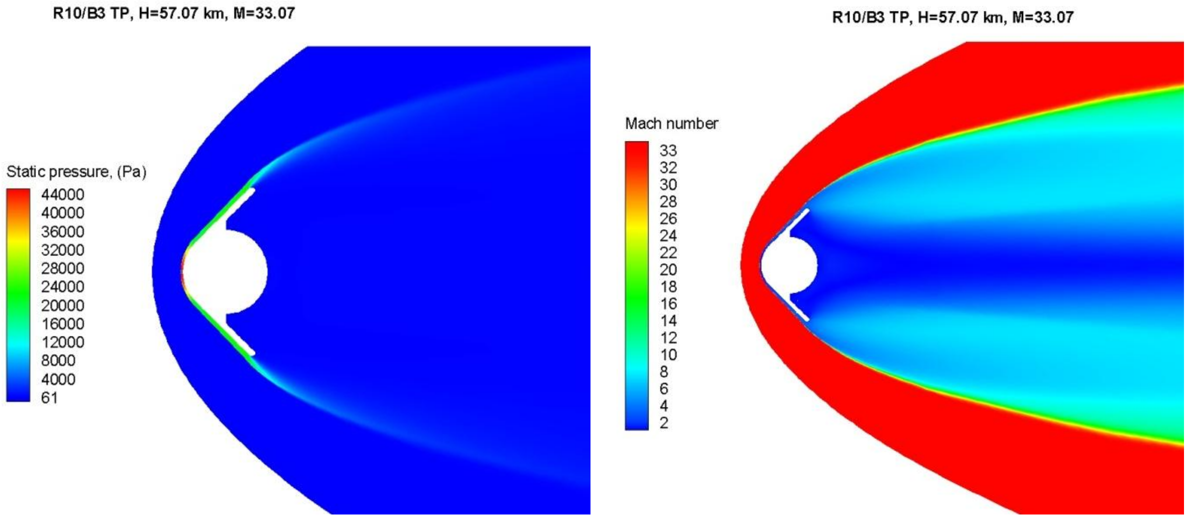

Figure 17. Mach number and static pressure contours field at R10/B3 TP.

The boundary layer, however, is significantly different with respect to the non-ablating cases [10]. Indeed, the species produced by the blowing along the stagnation streamline at R10/B3 TP are plotted in Figure 18.

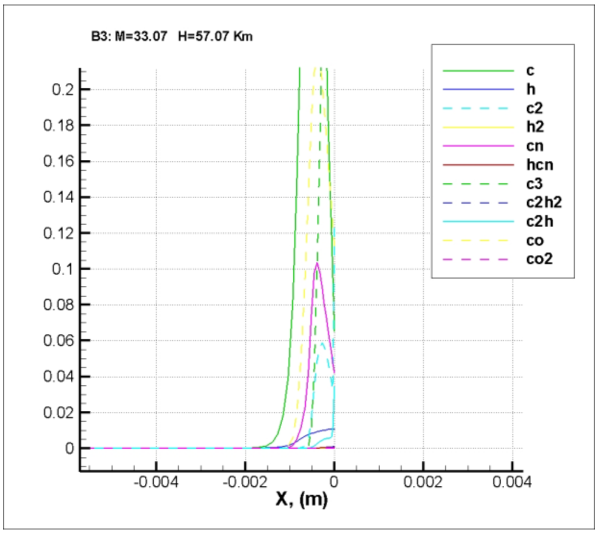

Figure 18. Ablation products on the stagnation streamline at R10/B3 TP

The level of all of the air species fall as the wall is approached and the presence of the blown gases becomes more dominant. The ablation products in the boundary layer mainly consist of H_2, C_2H, C_2H_2, CO, C, and H [10]. In particular, the level of C_3 falls rapidly as the distance from the body increases, because it dissociates to form C_2 and C, and also indirectly leads to the formation of CN and HCN. However, the rise in the level of C in the boundary layer is mainly attributable to the dissociation of CO. The relatively slow rate at which the level of H falls with increasing distance from the wall suggests that either H_2 or alternatively some of the hydrocarbons present are dissociating [10].
Figure 19 and Figure 20 highlight C_2, C_3 and C, CO mass fractions field past the SRV, respectively.

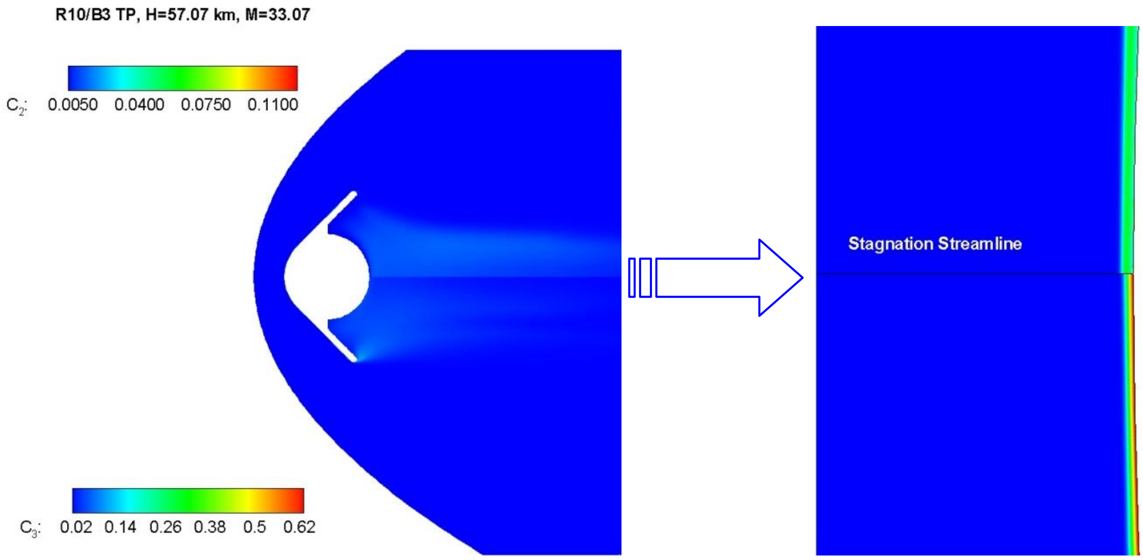

Figure 19. C2 and C3 mass fractions at R10/B3 TP.

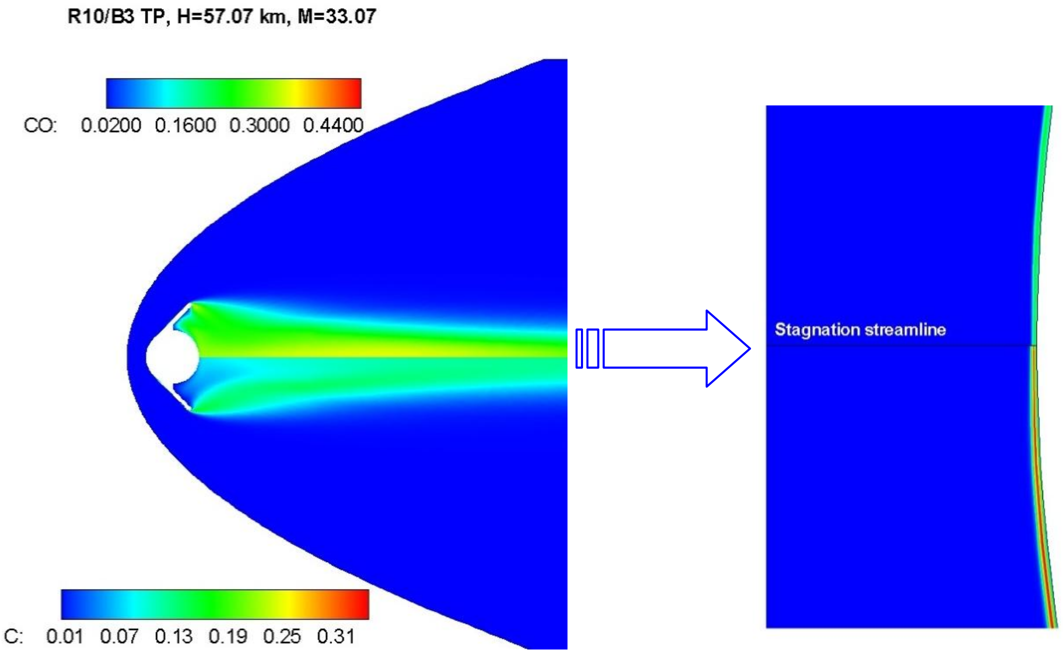

Figure 20. C and CO mass fractions at R10/B3 TP.

Note that the determination of the distribution of the products of the ablation process within the shock layer is very important since species such as C_2, C_3 and also CO have strong radiative properties. In particular, C_2 and C_3 possess absorption properties while CO is a strong radiator.

Finally, a summary review of SRV aerodynamics is shown in term of lift (C_L), drag (C_D), and pitching moment (C_M) coefficients (only drag in CFD analysis) that are calculated considering S_{ref} =0.95 m^2 (i.e., maximum SRV cross section area), L_{ref}=1.1 m (i.e., maximum SRV diameter) and pole at center-of-gravity, located at 26.5 % of diameter.

Figure 21 shows a typical mesh surface of SRV that has been used for the engineering-level computations, in which Surface Impact Methods (SIM) typical of hypersonics, such as Prandtl-Meyer expansion flow and Modified Newtonian theories are widely applied [9]. Analysis has been performed also in FMF conditions.

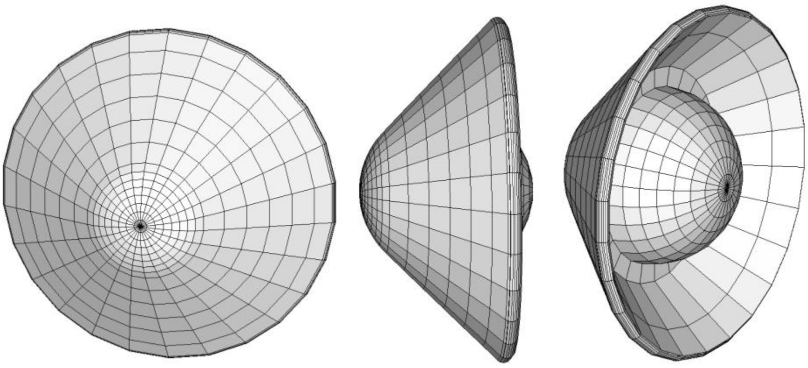

Figure 21. SRV panel mesh.

As an example of engineering level results, the static pressure distributions over the wetted vehicle surface for M_∞=25 and for two different angles of attack: 0, and 5 deg are summarized in Figure 22, respectively. As shown, when the AoA increases the surface pressure distribution changes thus increasing on the capsule windside, as expected. At the same time flow expansion on the capsule leeside determines locally lower pressure contours (see also Figure 7 and Figure 8).

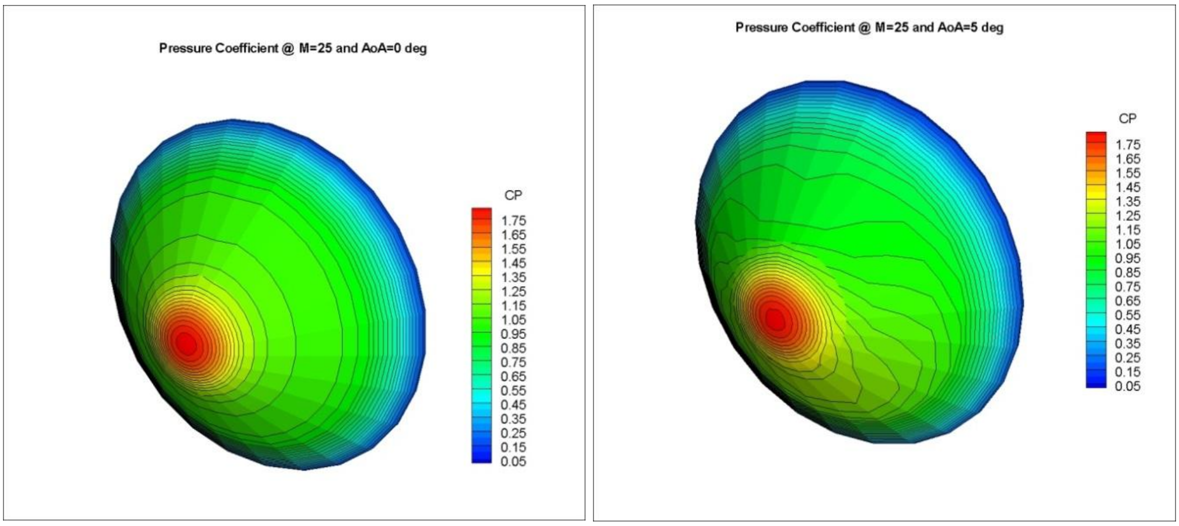

Figure 22. Pressure coefficient at M_∞=25 and AoA=0 and 5deg.

The lift, drag and pitching moment coefficients for AoA ranging from 0 to 180 deg, in hypersonic continuum conditions, are summarized in Figure 23. Note that results provided for aerodynamic drag agree with analytical results available for blunt cone at hypersonic speed [1]. Moreover, preliminary SRV aerodynamics summarized in Figure 23 provide also information about aerodynamic backward static stability of the probe during hypersonic re-entry.

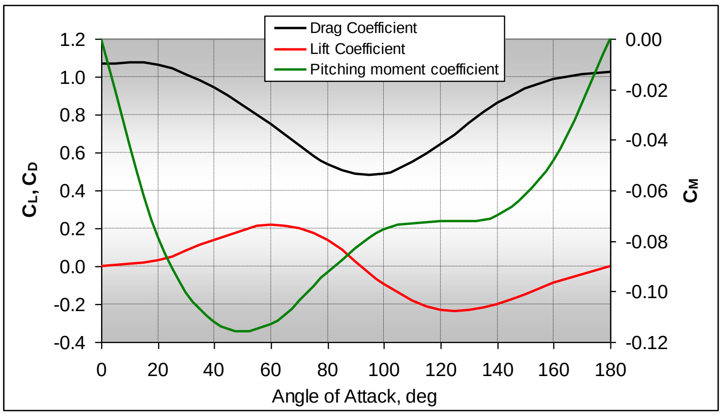

Figure 23. Lift, drag and pitching moment coefficients of SRV in hypersonic continuum regime.

As illustrated in Figure 23, the chosen aeroshape has two trim angles-of-attack where the pitching moment at the center of gravity is equal to zero (C_M=0 at AoA=0 deg and 180 deg). But, for the 180 deg AoA, the slope of the pitching coefficient ($C_{M\alpha}$) is positive and consequently the aeroshape has only one single stable position for AoA=0 deg. This ensures that the probe will not perform a backward re-entry in hypersonic regime.

Capsule drag coefficients evaluated for all performed CFD computations are summarized in Table 2. As one can see, drag break-down is also reported for those computations performed for whole flowfield domain for the SRV front shield (FS) and back shield (BS).

At very high Mach number conditions, there is a negligible effect of BS on the drag coefficient estimation as expected. This is due to the fact that the greater contribution to this coefficient is represented by the wave drag due to the pressure acting on the SRV forebody. Comparison among present CFD results and literature data is shown in Figure 24 [1]. It presents an approximation of the drag coefficient across the Mach range for the 45-degree half-angle shape. The hypersonic value, 1.07, was computed at Mach 31.8 and 21.5 using the Langley Aerothermodynamic Upwind Relaxation Algorithm (LAURA) [1]. The subsonic value, 0.65, comes from tests conducted in the Langely 20-foot Vertical Spin Tunnel. The supersonic and transonic values are from Brooks and Nichols wind tunnel data on a similar geometry.

Table 2: SRV drag coefficients

			Drag Coefficient				
			CDf		CDp		CDtot
Points	Mach	Mesh	FS	BC	FS	BS	
M1	**34.45**	**FS**	0.0131	na*	1.0196	na	1.0327
M2	**29.12**	**FS**	0.0072	na	1.0219	na	1.0291
M3	**25.11**	**FS**	0.0055	na	1.0269	na	1.0324
M4	**17.61**	**FS+BS**	0.0041	0.0004	1.0276	0.0029	1.0350
M5	**7.00**	**FS+BS**	0.0031	0.0008	1.0436	0.0204	1.0679
M6	**3.02**	**FS+BS**	0.0024	0.0010	1.1570	0.1111	1.2716
M1a	**34.45**	**FS**	0.0117	na	1.0145	na	1.0262
M2a	**29.12**	**FS**	0.0074	na	1.0242	na	1.0316
M3a	**25.11**	**FS**	0.0056	na	1.0270	na	1.0326
M4a	**17.61**	**FS+BS**	0.0042	0.0003	1.0326	0.0027	1.0399
M5a	**7.00**	**FS+BS**	0.0032	0.0006	1.0490	0.0208	1.0736
M6a	**3.02**	**FS+BS**	0.0025	0.0010	1.1657	0.1123	1.2815
R1	**41.54**	**FS**	0.0206	na	1.0092	na	1.0298
R2	**37.45**	**FS**	0.0155	na	1.0095	na	1.0250
R3	**34.45**	**FS**	0.0131	na	1.0196	na	1.0327
R4	**32.16**	**FS**	0.0101	na	1.0172	na	1.0273
R5	**29.12**	**FS**	0.0072	na	1.0219	na	1.0291
R6	**25.11**	**FS**	0.0055	na	1.0269	na	1.0324
R7	**40.14**	**FS**	0.0231	na	1.0133	na	1.0364
R8	**38.70**	**FS**	0.0196	na	1.0121	na	1.0317
R9	**35.87**	**FS**	0.0138	na	1.0107	na	1.0245
R10	**33.07**	**FS**	0.0114	na	1.0170	na	1.0284
R11	**30.50**	**FS**	0.0087	na	1.0203	na	1.0290
R12	**22.07**	**FS**	0.0070	na	1.0283	na	1.0353
B1	**41.54**	**FS**	0.0048	na	1.0390	na	1.0438
B2	**37.45**	**FS**	0.0133	na	1.0108	na	1.0241
B3	**33.07**	**FS**	0.0135	na	1.0134	na	1.0269
B4	**29.12**	**FS**	0.0052	na	1.0221	na	1.0273
B5	**25.11**	**FS**	0.0056	na	1.0256	na	1.0312
B6	**17.61**	**FS**	0.0043	na	1.0267	na	1.0310
B7	**10.10**	**FS**	0.0040	na	1.0306	na	1.0346
B8	**7.00**	**FS**	0.0009	na	1.0459	na	1.0468

For the purposes of this feasibility study, the important data are the hypersonic value, which affects the heat pulse, and the subsonic value that determines the impact velocity [1].

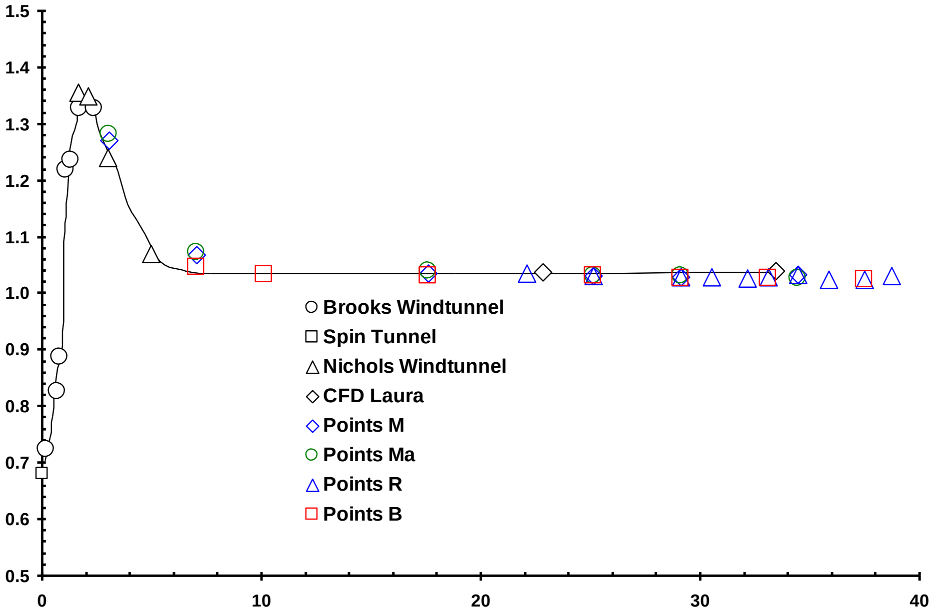

Figure 24. Drag coefficient of SRV comparison among present and literature results [1]

The drag coefficients of the present evaluation compare rather well with literature data, especially at very high Mach number flow conditions. Below Mach 7, forebody-only CFD will not accurately predict the aerodynamics. The calculations must include the afterbody and wake. Therefore, differences are recognized at rather low Mach number. In this cases, the effect of base drag could be arose as one can see looking at the difference in back shell configuration between SRV and the capsule considered in the literature data shown in Figure 25 [1].

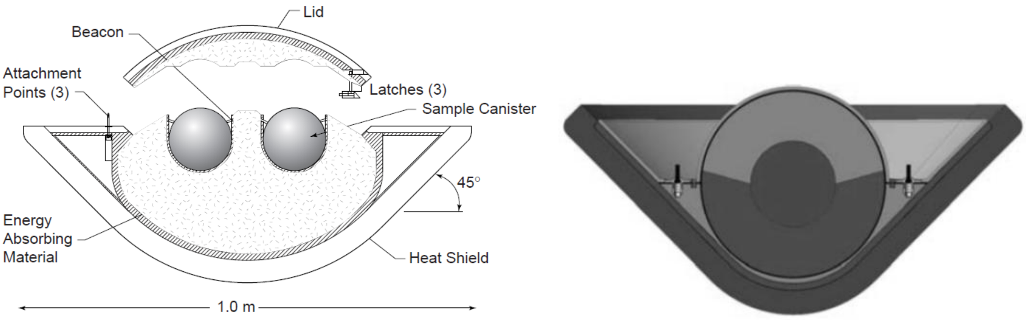

Figure 25. SRV configuration comparison [1]

3. Conclusion

In this work, numerical simulations have been carried out for a super-orbital re-entry capsule. A design analysis was performed to determine both aerodynamic and aerothermodynamic performances of an entirely passive Earth entry capsule for sample return mission. In particular, this work is useful to assess the aerodynamic performances and stability along the entry trajectory path, and to elaborate and validate an engineering tool that couples: aeroshape aerodynamic; trajectory and stability; aerothermal environments and heat shield ablation.

Present design result refers to both numerical and engineering-based analysis of a 1.1 m diameter spherically-blunted 45-deg half-angle forebody with a low-density, ablative heatshield.

Engineering-based design has been applied to assess flow field regime and capsule aerodynamics; while Navier-Stokes simulations have been performed to evaluate flow field past the capsule to perform flow plasma radiation analysis and effects of heat shield mass blowing. Results of the analysis are presented and discussed.

References

[1] Mitcheltree, R. A., Kellas, S., Dorsey, J. T., Desai, P. N., Martin, C.J., “A passive Earth-Entry Capsule for Mars Sample Return.” 51st International Astronautics Federation Congress, Rio de Janeiro. 1998. IAF-00-Q.3.04.

[2] Scott, C. D., Ried, R. C., Maraia, R. J., Li, C. P., and Derry, S. M., "An AOTV Aeroheating and Thermal Protection Study,” H. F. Nelson (ed.), Thermal Design of Aeroassisted Orbital Transfer Vehicles, Vol. 96 of Progress in Astronautics and Aeronautics, AIAA,New York, 1985, pp. 198-229.

[3] Tauber M. E. and Suttont, K.,“Stagnation-Point Radiative Heating Relations for Earth and Mars Entries,” Journal of Spacecraft and Rockets. Vol. 28, No. 1, pp. 40-42.

[4] PLASMA RADIATION DATABASE PARADE V2.2. Report TR28/96

[5] USV_X-Phase A Aerodynamic and Aerothermodynamic Analysis. Report CIRA-CF-06-1393.

[6] CLAE Project. H3NS: Code Development Verification and Validation. Report CIRA-CF-06-1017.

[7] Anderson J., Hypersonic and High Temperature Gas Dynamics. McGraw-Hill Book Company, New York 1989

[8] Review of Chemical Kinetic Problems of Future NASA Missions: Earth Entries. Journal of Thermophysics and Heat Transfer Vol 7. No 3. 1993.

[9] Bertin,J., Hypersonic Aerothermodynamics. AIAA Educational Series, Washington. 1994

[10] Roberts, T. P, “Modelling Gas/Surface Interaction Processes of Ablating Wall Boundaries Associated with Planetary Entry,”, Proceedings of the 2nd European Symposium Aerothermodynamics for space vehicles, Noordwijk, The Netherlands, 21-25 November, 1994, European Space Agency (ESA) (Paris), 1995, p. 311.

[11] Notes on Earth Atmospheric Entry for Mars Sample Return Missions. NASA/TP–2006-213486. 2006